CM^2 Magazine

第 128 期

南方科技大学海洋磁学中心主编

https://cm2.sustech.edu.cn/

创刊词

海洋是生命的摇篮，是文明的纽带。地球上最早的生命诞生于海洋，海洋里的生命最终进化成了人类，人类的文化融合又通过海洋得以实现。人因海而兴。

人类对海洋的探索从未停止。从远古时代美丽的神话传说，到麦哲伦的全球航行，再到现代对大洋的科学钻探计划，海洋逐渐从人类敬畏崇拜幻想的精神寄托演变成可以开发利用与科学研究的客观存在。其中，上个世纪与太空探索同步发展的大洋科学钻探计划将人类对海洋的认知推向了崭新的纬度：深海（deep sea）与深时（deep time）。大洋钻探计划让人类知道，奔流不息的大海之下，埋藏的却是亿万年的地球历史。它们记录了地球板块的运动，从而使板块构造学说得到证实；它们记录了地球环境的演变，从而让古海洋学方兴未艾。

在探索海洋的悠久历史中，从大航海时代的导航，到大洋钻探计划中不可或缺的磁性地层学，磁学发挥了不可替代的作用。这不是偶然，因为从微观到宏观，磁性是最基本的物理属性之一，可以说，万物皆有磁性。基于课题组的学科背景和对海洋的理解，我们对海洋的探索以磁学为主要手段，海洋磁学中心因此而生。

海洋磁学中心，简称 CM^2，一为其全名“Centre for Marine Magnetism”的缩写，另者恰与爱因斯坦著名的质能方程 $E = MC^2$ 对称，借以表达我们对科学巨匠的敬仰和对科学的不懈追求。

然而科学从来不是单打独斗的产物。我们以磁学为研究海洋的主攻利器，但绝不仅限于磁学。凡与磁学相关的领域均是我们关注的重点。为了跟踪反映国内外地球科学特别是与磁学有关的地球科学领域的最新研究进展，海洋磁学中心特地主办 CM^2 Magazine，以期与各位地球科学工作者相互交流学习、合作共进！

“海洋孕育了生命，联通了世界，促进了发展”。21 世纪是海洋科学的时代，由陆向海，让我们携手迈进中国海洋科学的黄金时代。

目 录

1. 浮游植物的垂向移动刺激海洋初级生产力的勃发

翻译人：仲义 zhongy@sustech.edu.cn

Wirtz, K., Smith, S.L., Mathis, M., et al., ***Vertical migrating phytoplankton fuel high oceanic primary production*** *[J]. Nature Climate Change, 2022, 12,750-756.*

https://doi.org/10.1038/s41558-022-01430-5

摘要：由于光照深度和养分充足深度之间的垂直具体分别为 50-150 米使得海洋净初级生产力（NPP）非常高。本文，作者的证据表明，许多自养生物通过向下和向上的迁移可以填补这一空白，从而促进了生物养分的输送和海洋 NPP 的高速率。模型结果表明，浮游植物垂向迁移可产生高达 40%的新产物，并直接贡献了海洋总 NPP 的 25%。NPP 的季节性、垂直和地理变化的良好再现支持了这些估计的可信度。与常见的预测相反，垂向混合模式的敏感性研究表明，在全球变暖的情况下，当层结增强较少，海洋表面的物理营养输送，NPP 会更高。研究结果表明，浮游植物垂向移动是推动海洋生物地球化学的关键机制，因此，需要考虑全球碳收支平衡。

ABSTRACT: Marine net primary production (NPP) is remarkably high given the typical vertical separation of 50-150 m between the depth zones of light and nutrient sufficiency, respectively. Here we present evidence that many autotrophs bridge this gap through downward and upward migration, thereby facilitating biological nutrient pumping and high rates of oceanic NPP. Our model suggests that phytoplankton vertical migration (PVM) fuels up to 40% (>28 tg yr^{-1} N) of new production and directly contributes 25% of total oceanic NPP (herein estimated at 56 PgC yr^{-1}). Confidence in these estimates is supported by good reproduction of seasonal, vertical and geographic variations in NPP. In contrast to common predictions, a sensitivity study of the PVM model indicates higher NPP under global warming when enhanced stratification reduces physical nutrient transport into the surface ocean. Our findings suggest that PVM is a key mechanism driving marine biogeochemistry and therefore requires consideration in global carbon budgets.

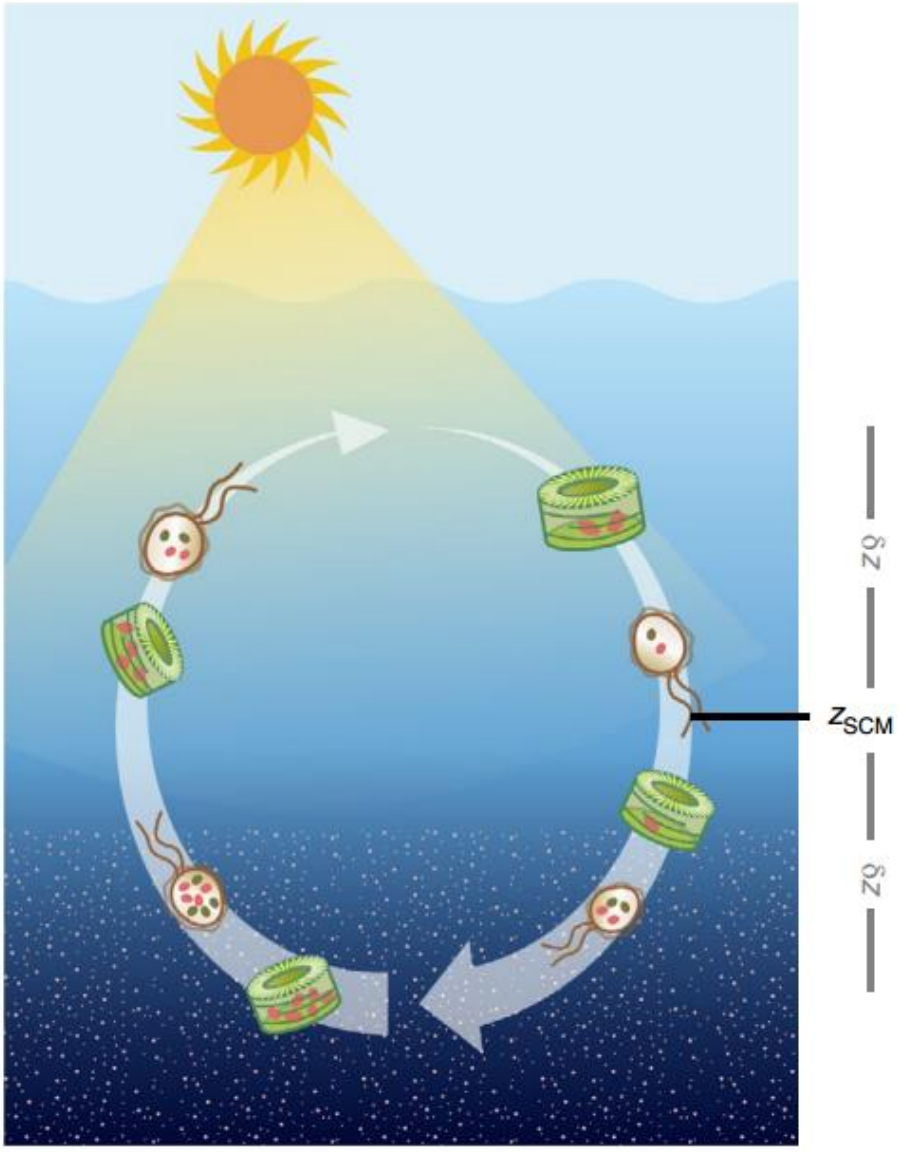

Figure 1. Biological nutrient pumping by vertically migrating phytoplankton cells. Cells with low intracellular nutrient content (indicated by small ellipses) settle or swim down to the chemocline while nutrient-rich cells ascend to the sunlit surface layers. Their vertical habitat spans from $z_{SCM} - \delta z$ to $z_{SCM} + \delta z$ with the average position z_{SCM} marking the depth of the subsurface chlorophyll maximum and vertical distance δz the migration amplitude. The up and down migration leads to a separation of cells having low versus high nutrient/C ratios at the same depth, depending only on their migration history. This separation is difficult to observe in situ and impossible to resolve in the Eulerian grid representation of conventional BGC models.

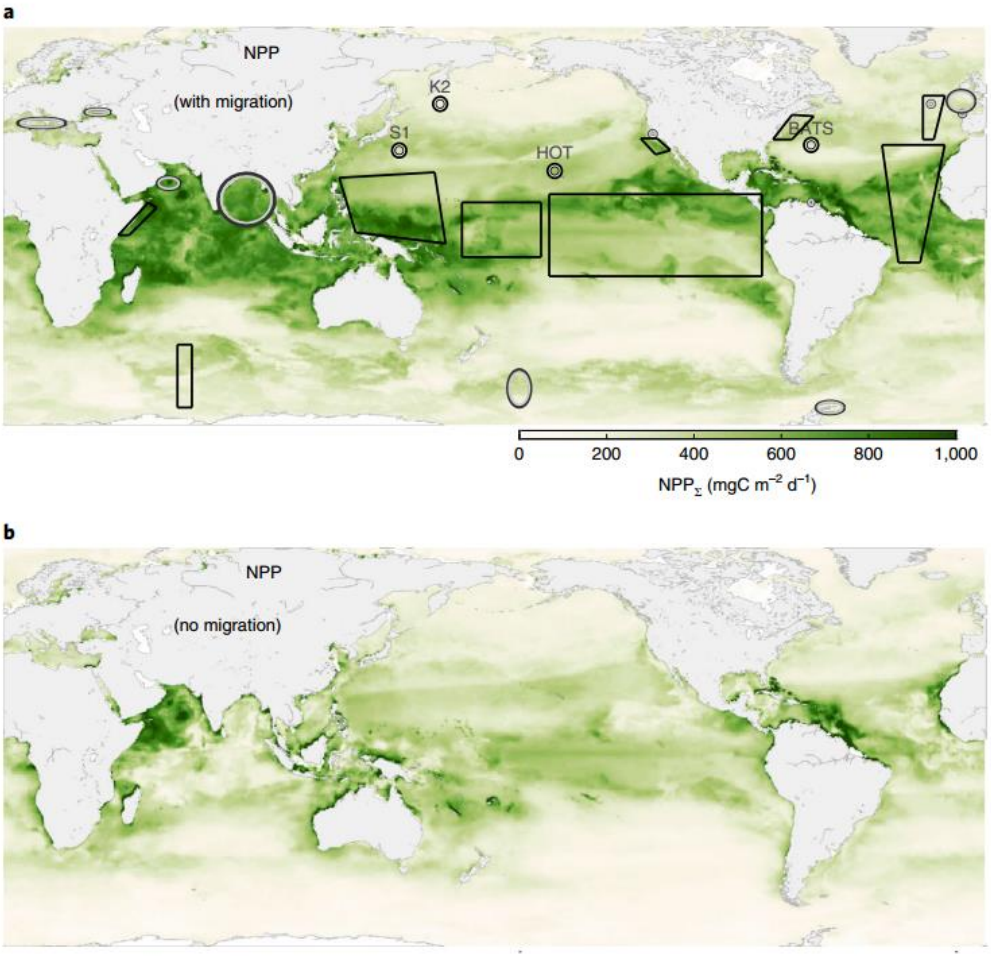

Figure 2. Simulated annual NPPΣ. a, NPP Σ calculated with PVM switched on. b, NPP Σ with PVM switched off. These applications were fed by global fields of incident surface light, water temperature and chemocline depth (Methods). Circles, ellipses and polygons in a mark time-series stations and monitored areas referenced in the model–data comparison in Extended Data Fig. 2.

2. Kamchatka 弧下的脱水流体来源

翻译人：周洋 zhouy3@sustech.edu.cn

Ghu Y C, Sune G G, Veronique L R et al. ***Sources of dehydration fluids underneath the Kamchatka arc*** *[J]. Nature Communications, 2022, 13:4467.*

https://doi.org/10.1038/s41467-022-32211-5

摘要：俯冲板片物质的运移及岛弧岩浆的产生与流体活动密切相关体。目前，俯冲过程中产生的流体，其来源仍然存在争议。Kamchatka 弧因为弧岩浆具有高铁镁质特征，来源基本上不含俯冲过程中沉积物的加入，因此是识别流体来源的理想俯冲带。俯冲的夏威夷皇帝海山链（HESC）被认为为 Kamchatka 岩浆活动提供大量流体。本文研究表明 Tl 同位素可以示踪 HESC 对 Kamchatka 弧岩浆的贡献。结合微量元素比值和文献数据，我们示踪了 Kamchatka 弧俯冲的 HESC 脱水和熔融过程。蛇纹石（<100 公里深度）、硬柱石（100-250 公里深度）和白云母（>250 公里深度）依次分解并产生有利于东部火山前缘（EVF）、Kamchatka 中部凹陷（CKD)及和 Sredinny 岭(SR)岩浆作用的流体。然而，鉴于蛇纹石和硬柱石流体具有低 Tl 特征，俯冲的 HESC 来解释在 EVF 和 CKD 熔岩中观察到的 HESC 一样的 Tl 同位素特征。在 Kamchatka 弧地区没有榴辉岩地壳熔融过程的情况下，我们建议以 HESC 为主的混杂岩逐渐脱水和熔融，为同位素和微量元素组合数据提供了最令人信服的解释。

ABSTRACT: Fluids mediate the transport of subducted slab material and play a crucial role in the generation of arc magmas. However, the source of subduction-derived fluids remains debated. The Kamchatka arc is an ideal subduction zone to identify the source of fluids because the arc magmas are comparably mafic, their source appears to be essentially free of subducted sediment-derived components, and subducted Hawaii-Emperor Seamount Chain (HESC) is thought to contribute a substantial fluid flux to the Kamchatka magmas. Here we show that Tl isotope ratios are unique tracers of HESC contribution to Kamchatka arc magma sources. In conjunction with trace element ratios and literature data, we trace the progressive dehydration and melting of subducted HESC across the Kamchatka arc. In succession, serpentine (<100 km depth), lawsonite (100–250 km depth) and phengite (>250 km depth) break down

and produce fluids that contribute to arc magmatism at the Eastern Volcanic Front (EVF), Central Kamchatka Depression (CKD), and Sredinny Ridge (SR), respectively. However, given the Tl-poor nature of serpentine and lawsonite fluids, simultaneous melting of subducted HESC is required to explain the HESC-like Tl isotope signatures observed in EVF and CKD lavas. In the absence of eclogitic crust melting processes in this region of the Kamchatka arc, we propose that progressive dehydration and melting of a HESC-dominated mélange offers the most compelling interpretation of the combined isotope and trace element data.

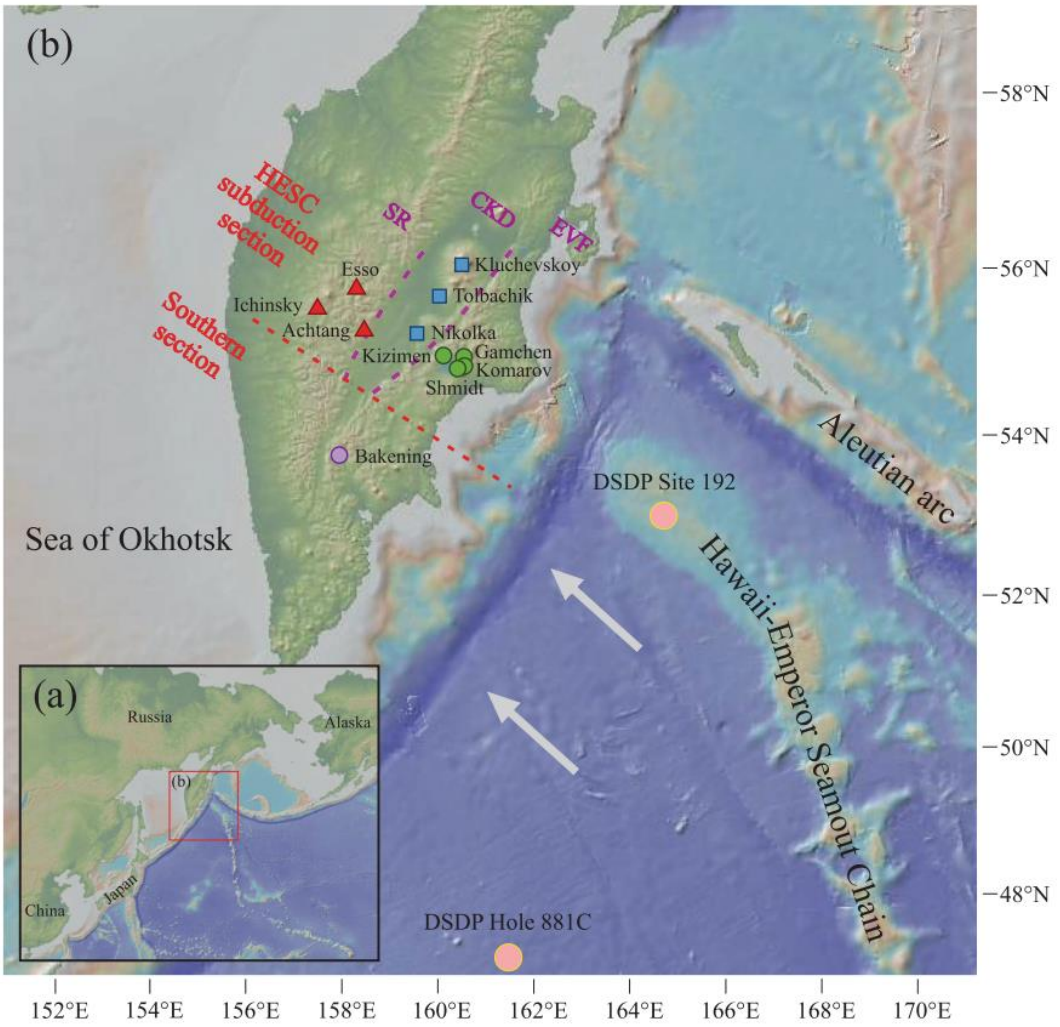

Figure 1. Location of Kamchatka subduction zone. a Location of Kamchatka arc and surrounding areas. b Map of the Kamchatka arc and Hawaii-Emperor Seamount Chain (HESC). Solid circle, square and triangle indicate the sampled volcanoes from Eastern Volcanic Front (EVF), Central Kamchatka Depression (CKD) and Sredinny Ridge (SR), respectively. Also shown is the location of two drill cores from which samples were analyzed in this study to constrain the sediment and HESC input flux to the

arc. Approximate plate motion direction is represented by arrows[24]. Perpendicular to the plate motion direction, Kamchatka arc was divided into two sections: HESC subduction zone (EVF, CKD and SR); south of HESC subduction zone (Bakening volcano indicated by purple circle).

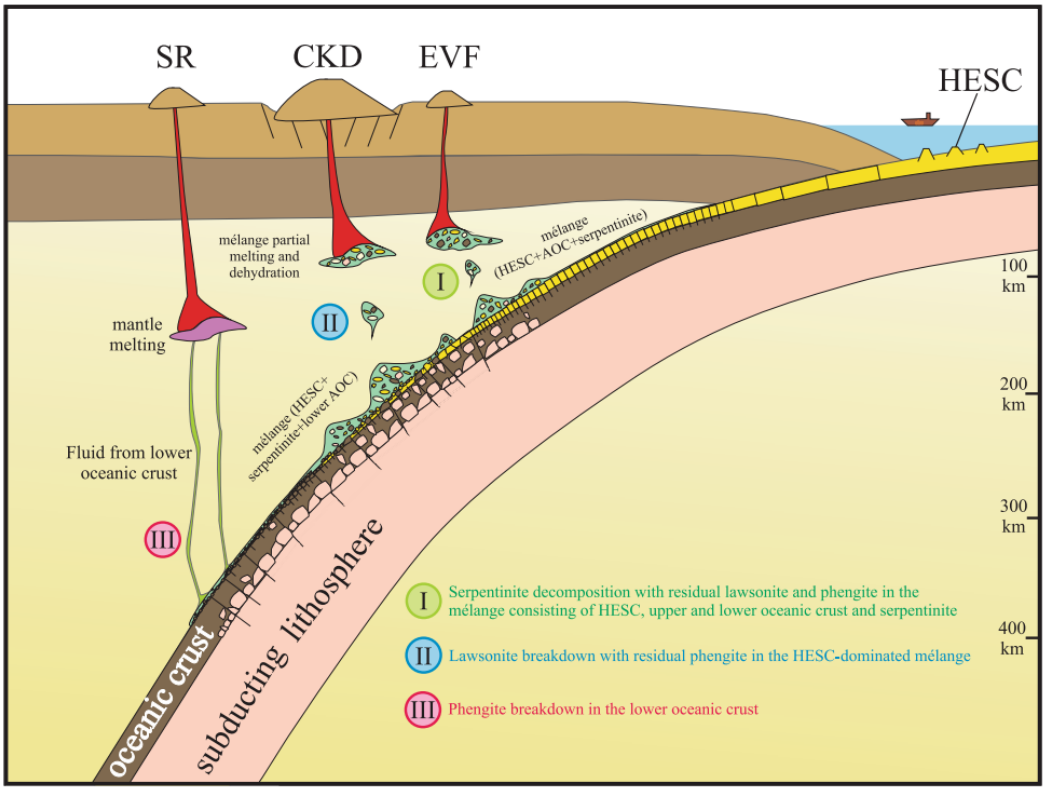

Figure 2. Cartoon of the mélange model of slab material transport in Kamchatka subduction zone. (I) Below Eastern Volcanic Front (EVF), the mélange contains Hawaii-Emperor Seamount Chain (HESC), upper and lower oceanic crust and serpentinite. Decomposition of serpentine with residual lawsonite and phengite in the mélange account for the highest fluid-mobile chalcophile trace element concentrations and $\delta^{11}B$ values as well as Cs/U, Cs/Pb and B/Nb, together with relatively high Cs/Tl and U/K and low Sr/Nd and Ba/Th. (II) Underlying Central Kamchatka Depression (CKD), the mélange consists of HESC, serpentinite and/or lower oceanic crust. Breakdown of hydrous lawsonite and residue of phengite in the HESC of the mélange results in relatively low Ba/Th and Sr/Nd and high Cs/Tl, U/K and Pb/Tl in CKD lavas. (III) Beneath Sredinny Ridge (SR), the HESC-rich mélange layer was substantially mobilized before fluids contributing to SR are released. Breakdown of phengite in the lower oceanic crust results in high Ba/Th and Sr/Nd and low Cs/Tl, U/K and Pb/Tl in SR lavas. See discussion for details.

3. 加拿大 Simcoe 湖约 14000 年的环境变化记录

翻译人：张靖宇 zhangjy6@sustech.edu.cn

R.M. Doyle, N. Bumstead, C.F.M. Lewis, et al. ***A ~14 000-year record of environmental change from Lake Simcoe, Canada*** *[J]. Quaternary Science Reviews, 2022.*

https://doi.org/10.1016/j.quascirev.2022.107667

摘要：虽然对 Laurentian 大湖区的演变进行了深入研究，但专注于重建南安大略第四大湖--Simcoe 湖的历史的研究较少。本研究利用湖泊沉积物中包含的代理数据来重建 Simcoe 湖盆地 14000 年的古环境变化历史。首先，利用介形虫的氧同位素组成（$\delta^{18}O_{valve}$）来估计古湖水的氧同位素组成，$\delta^{18}O_{lake\ water}$。在 Simcoe 湖，$\delta^{18}O_{lake\ water}$ 对湖面的变化不敏感，但对温度的变化很敏感，可以捕捉到诸如全新世早期变暖的时期。这个 $\delta^{18}O_{lake\ water}$ 记录表明，从 Algonquin 湖向 Simcoe 湖输送融水的速度在 12050 cal yr BP 时开始减慢，支持以前基于地球物理数据的研究。它还表明，来自早期 Mattawa 湖的富含 ^{16}O 水的孤立脉冲可能发生在 ~10 699 至 10591 cal yr BP。下一步，利用介形虫的稳定碳同位素组成（$\delta^{13}C_{valve}$）来估计 Simcoe 中溶解的无机碳的稳定碳同位素组成（$\delta^{13}C_{DIC}$）。这些数据与介形虫种属、粒径、磁化率（MS）和沉积物矿物学相结合，支持我们对 $\delta^{18}O_{lake\ water}$ 温度敏感变化的解释，并提供了对湖内状况的进一步了解。8300~8000 cal yr BP 之间堆积速率的明显增加，以及粒径和陆源碳酸盐含量的不明显增加，可能反映了在 8200 cal yr BP 时 Laurentide Ice Sheet（LIS）的崩溃导致的从寒冷和干燥到湿润和温暖环境的突然转变。总之，这项研究完善了我们对 Simcoe 湖演变的理解，并提供了过去约 14000 年环境变化的全貌。

ABSTRACT: While the evolution of the Laurentian Great Lakes has been researched intensively, fewer studies have focused on reconstructing the history of Lake Simcoe, the fourth largest lake wholly within southern Ontario. This study uses proxy data, including ostracod valves, contained in lake sediments to reconstruct a ~14 000-year history of paleoenvironmental change in the Lake Simcoe basin. First, oxygen-isotope compositions of ostracod valves ($\delta^{18}O_{valve}$) are used to estimate the oxygen-isotope composition of ancient lake water, $\delta^{18}O_{lake\ water}$. In Lake Simcoe, $\delta^{18}O_{lake\ water}$ is insensitive to changes in lake level but sensitive to shifts in temperature, capturing periods such as

the early Holocene warming. This $\delta^{18}O_{lake\ water}$ record demonstrates that the delivery of meltwater from Lake Algonquin to Lake Simcoe began to slow at ~12 050 cal yr BP, supporting previous research based on geophysical data. It also suggests that an isolated pulse of ^{16}O-rich water from Early Lake Mattawa may have occurred from ~10 699 to 10 591 cal yr BP. Next, stable carbon-isotope compositions of ostracod valves ($\delta^{13}C_{valve}$) are used to estimate the stable carbon-isotope composition of dissolved inorganic carbon ($\delta^{13}C_{DIC}$) in Lake Simcoe. These data, combined with ostracod assemblages, grain size, magnetic susceptibility (MS) and sediment mineralogy, support our interpretation of temperature-sensitive variation in $\delta^{18}O_{lake\ water}$ and provide further insights into in-lake conditions. A pronounced increase in accumulation rate, and subtler increases in grain size and detrital carbonate contents, between ~8300 and ~8000 cal yr BP may reflect the abrupt transition from cold and dry to wet and warm conditions resulting from the collapse of the Laurentide Ice Sheet (LIS) at ~8200 cal yr BP. In summary, this study refines our understanding of the evolution of Lake Simcoe and provides a holistic picture of environmental change over the last ~14 000 years.

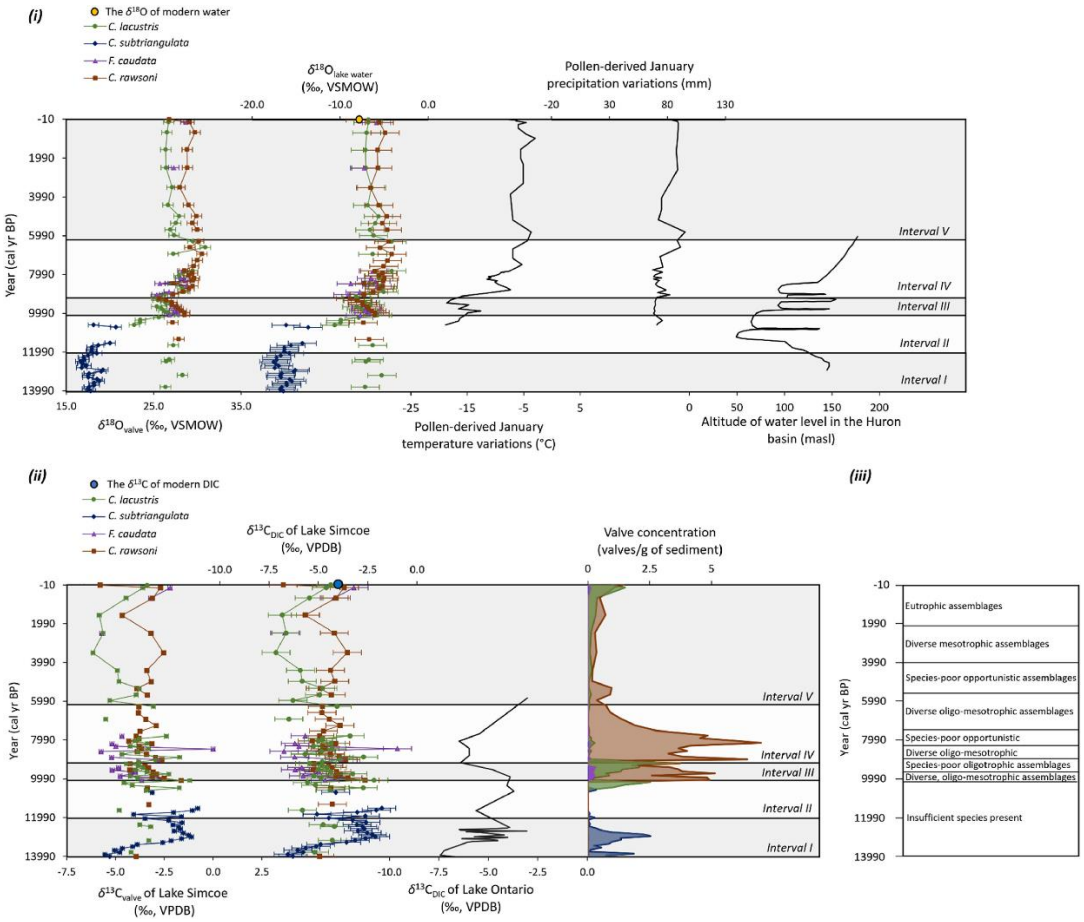

Figure 1. Proxies derived from ostracods in core PC-5 from Lake Simcoe compared with previously published records. Panel ***(i)*:** The $\delta^{18}O_{valve}$ and $\delta^{18}O_{lake\ water}$ for ostracods from PC-5 compared with January temperature and precipitation reconstructions derived from pollen assemblages in PC-5 (Volik et al., 2016) and the altitude of water level in the Huron Basin (Lewis and Anderson, 2012, Lewis et al., 2005). January temperatures were used in the absence of any other temperature data. For ostracod data, each datapoint represents a bulk sample containing 5–6 valves. Note that the $\delta^{18}O$ of modern lake water overlaps with (and therefore conceals) the youngest estimate of $\delta^{18}O_{lake\ water}$ derived from *C. rawsoni*. **Panel *(ii)*:** The $\delta^{13}C_{valve}$ and $\delta^{13}C_{DIC}$ of ostracods from PC-5 compared with trends in $\delta^{13}C_{DIC}$ from Lake Ontario (Hladyniuk and Longstaffe, 2015). The illustrated values for $\delta^{18}O_{valve}$ and $\delta^{13}C_{valve}$ have not been corrected for vital effects, while estimates of $\delta^{18}O_{lake\ water}$ and $\delta^{13}C_{DIC}$ have been so corrected, as described in the methods. **Panel *(iii)*** A summary of trends in the assemblages of testate amoeba and non-pollen palynomorphs identified in Volik et al. (2016).

4. 热带和温带辐射驱动的补偿作用导致弱哈德莱环流强度变化

翻译人：杨会会 11849590@mail.sustech.edu.cn

Kim D, Kim H J, Kang S M, et al., ***Weak Hadley cell intensity changes due to compensating effects of tropical and extratropical radiative forcing [J].*** *Climate and atmospheric science. 2022,5, 61.*

https://doi.org/10.1038/s41612-022-00287-x

摘要：哈德莱环流对全球 CO_2 浓度增加的响应具有复杂的空间特征：上升支增强，下降支减弱。为了更好地理解这些变化，我们研究了哈德莱环流对不同纬度带理想辐射驱动的敏感性。哈德莱环流的反应在一阶上受驱动的纬度结构支配。上升支的增强是热带驱动的结果，而下降支的减弱是温带驱动的结果。大气涡旋热传输的变化放大了这些直接辐射驱动哈德莱环流的响应，而总湿（gross moist）稳定性和海洋热吸收的变化则部分抵消了这些响应。辐射反馈通过改变经向大气能量梯度进一步调节哈德莱环流的响应。因此，全球变暖下的哈德莱环流是热带和温带辐射驱动的相反作用，即补偿作用的结果。

ABSTRACT: The Hadley cell response to globally increasing CO_2 concentrations is spatially complex, with an intensified rising branch and weakened descending branch. To better understand these changes, we examine the sensitivity of the Hadley cell to idealized radiative forcing in different latitude bands. The Hadley cell response is, to first order, governed by the latitudinal structure of the forcing. The strengthening of the upward branch is attributed to tropical forcing, whereas the weakening of the descending branch is attributed to extratropical forcing. These direct radiatively-forced Hadley cell responses are amplified by changes in atmospheric eddy heat transport while being partially offset by changes in gross moist stability and ocean heat uptake. The radiative feedbacks further modulate the Hadley cell response by altering the meridional atmospheric energy gradient. The Hadley cell projections under global warming are thus a result of opposing - and thus compensating - effects from tropical and extratropical radiative forcings.

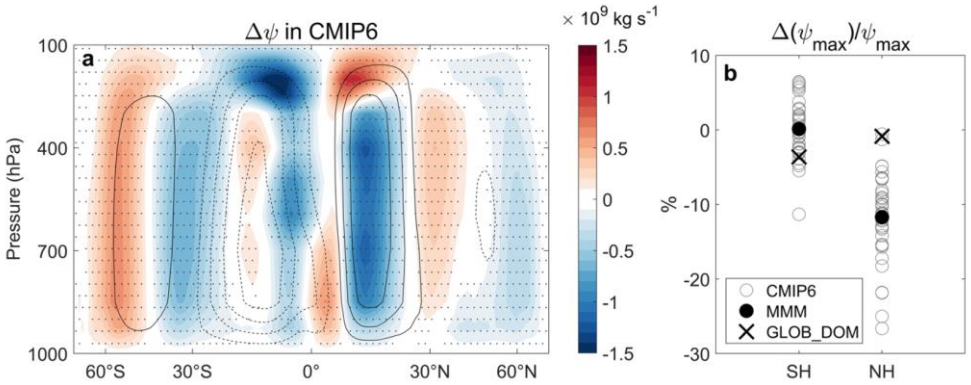

Figure 1. Hadley circulation responses to global CO_2 forcing in CMIP6. a Multi-model mean changes of the atmospheric annual-mean meridional stream function (shading; interval = 10^8 kg s^{-1}) averaged for years 11-60 after an abrupt global quadrupling of CO_2 concentrations from the corresponding pre-industrial control climatology averaged over the last 100 years (contours; interval = 2×10^{10} kg s^{-1}) for 40 CMIP6 models. Positive values (red shading and solid contours) correspond to a clockwise circulation and negative values (blue shading and dashed contours) to a counterclockwise circulation. Stippling indicates areas where at least two third of the models agree on the sign of the change. b Percentage changes of the southern and northern Hadley cell intensity (Δψmax=ψmax in %) averaged between 10°-20° latitude in each hemisphere. Each CMIP6 model response is shown with open circles, with the multi-model mean in black closed circles, and the GLOB_DOM experiment response indicated by black crosses.

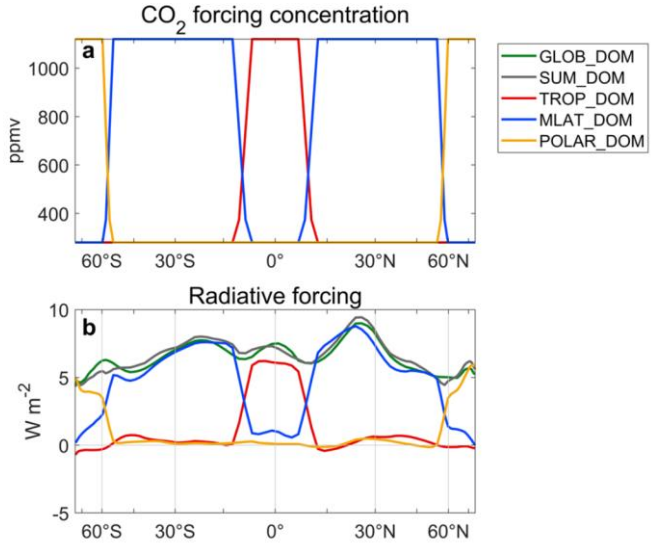

Figure 2. CO_2 forcing structures and radiative forcings. **a** The annualand zonal-mean profile of CO_2 concentration and **b** radiative forcing in GLOB_DOM (green), TROP_DOM (red), MLAT_DOM (blue), POLAR_DOM (yellow), and the sum of all regional forcing experiments SUM_DOM (gray).

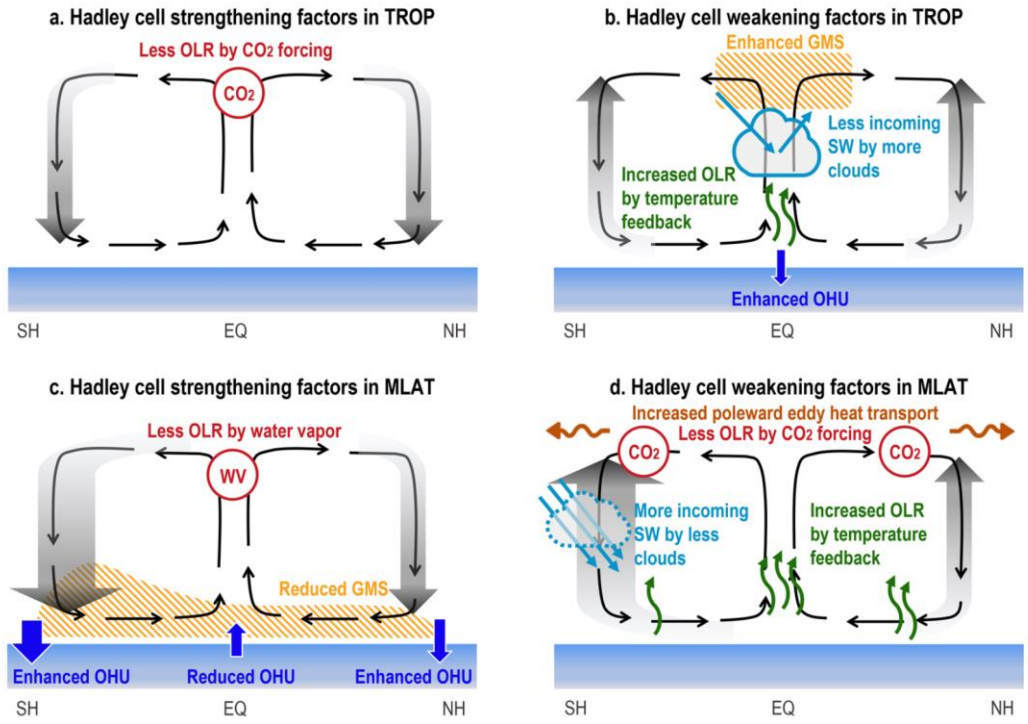

Figure 3. Schematic summary of the physical processes explaining the distinct HC responses to different CO_2 forcings. **a** Main factor that causes HC strengthening in response to TROP forcing is the direct CO_2 forcing that enhances the meridional atmospheric energy gradient. **b** HC weakening in response to TROP forcing is caused by the temperature feedback, shortwave cloud feedback, enhanced gross moist stability, and enhanced heat uptake by the equatorial ocean. **c** HC strengthening in response to MLAT forcing is caused by the water vapor feedback, reduced gross moist stability, and increased ocean heat uptake by the extratropical oceans and decreased ocean heat uptake by the equatorial ocean. **d** HC weakening in response to the direct CO_2 forcing in MLAT is amplified by enhanced poleward eddy heat transport, shortwave cloud feedback, and temperature feedback.

5. 赤铁矿作为印尼东加里曼丹 Jufri 洞穴中前所未有的黑色岩石艺术颜料：基于显微镜、光谱学和同步加速器 X 射线的研究

翻译人：曹伟 11930854@qq.com

Maryanti E, Ilmi M, Nurdini N. ***Hematite as unprecedented black rock art pigment in Jufri Cave, East Kalimantan, Indonesia: the microscopy, spectroscopy, and synchrotron X-ray-based investigation [J]****. Archaeological and Anthropological Sciences, 2022, 14, 122.*

https://doi.org/10.1007/s12520-022-01591-6

摘要：最近关于黑色颜料岩石艺术的研究报告称，全球各地的各种史前图像遗址是由碳化合物和锰氧化物组成。本研究中，我们报道了赤铁矿作为黑色颜料材料在岩石艺术中前所未有的使用。利用 SEM-EDS、XRF、SR-XRD、XANES、FTIR 以及拉曼光谱技术对东加里曼丹桑库利朗的 Jufri 洞穴红、紫、黑颜料材料的物理化学特征进行了详细的研究。结果表明，赤铁矿矿物是所有颜料原料的主要成分。然而，每种颜料中的赤铁矿晶体具有不同 Fe^{3+}离子的结晶性和八面体对称性。赤铁矿化合物的特征差异可能与高温加热过程有关，也可能与自然地质或人文因素有关。此外，赤铁矿结构中结晶度的差异和八面体对称性的差异可能是色素材料中赤铁矿晶体颜色变化的原因。通过这一研究获得的相关物理化学属性信息无疑为印尼岩石艺术的多样性颜料特征增添了新的见解。

ABSTRACT: Recent research on black pigment rock art reported on various prehistoric image sites globally consisting of carbon compounds and manganese oxides. In this paper, we report the unprecedented use of hematite as a black pigment material in rock art. Combination of scanning electron microscopy coupled with energy-dispersive X-ray spectrometry (SEM-EDS), X-ray fluorescence (XRF), synchrotron radiation X-ray diffraction (SR-XRD), X-ray absorption near-edge spectroscopy (XANES), Fourier transform infrared spectroscopy (FTIR), and Raman spectroscopy was able to provide detailed information on the physicochemical characteristics of red, purple and black pigment materials from Jufri Cave, Sangkulirang, East Kalimantan. The results show that the mineral hematite is the main component of all pigment materials. However, the

hematite crystals in each pigment possess different properties of crystallinity and octahedral symmetry of the Fe^{3+} ion. The characteristic differences in hematite compounds are possibly due to the high-temperature heating process and could be caused by natural geological or anthropological factors. Besides, the discrepancy of crystallinity and distortion of octahedral symmetry in the hematite structures are presumably responsible for the color variety among hematite crystals in the pigment material. The information on the physicochemical properties obtained from this research certainly adds new insights into the characteristics of pigments in the diversity of rock art in Indonesia.

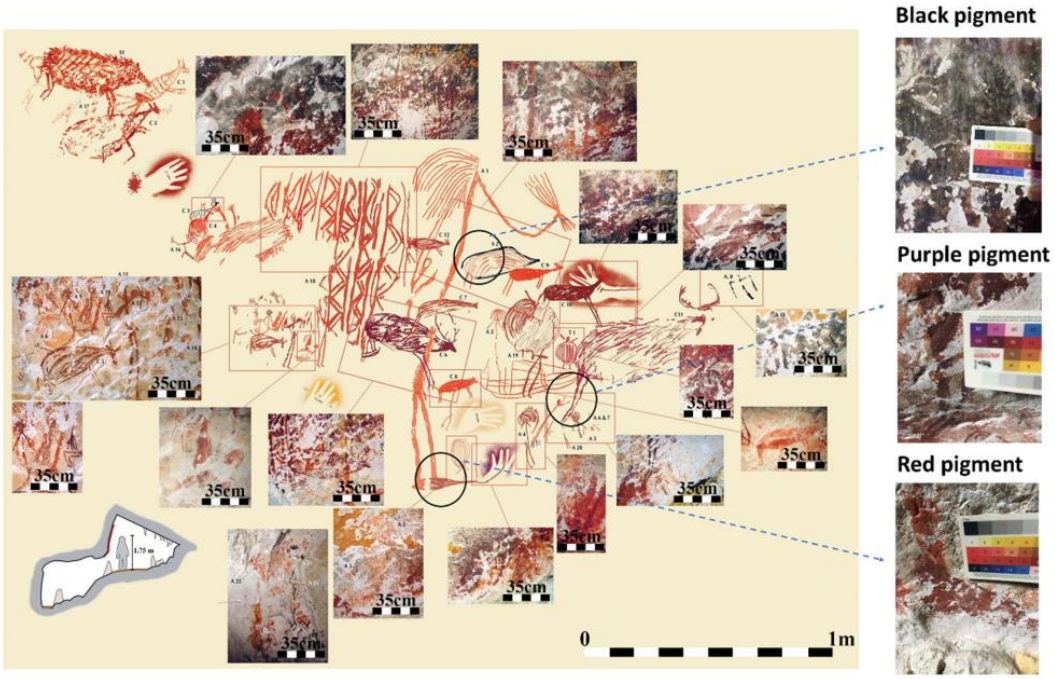

Figure 1. The illustration of painted panels with various image motifs (Fage et al. 2010) and the position of pigment samples collected from the Jufri Cave site

6. 末次冰消期印度季风区千年尺度的水汽变化

翻译人：王浩森 11930841@mail.sustech.edu.cn

Shi X, Liu S, Zhang X, et al. ***Millennial-scale hydroclimate changes in Indian monsoon realm during the last deglaciation****[J]. Quaternary Science Reviews, 2022, 292: 107702.*

https://doi.org/10.1016/j.quascirev.2022.107702

摘要：在印度季风区域，水气对北大西洋冰川突变气候事件的空间均一性及其潜在机制存在争议。在这里，我们重建了安达曼海中部过去 26000 年的海表面温度（SST）和海水氧同位素（$\delta^{18}O_{sw}$），以研究热带印度洋千年尺度气候变化的潜在驱动机制。我们的结果表明，末次冰消期的 SST 和 $\delta^{18}O_{sw}$ 的千年尺度变化与北大西洋气候变化之后的亚洲季风系统有关。特别是，在从 BØlling/AllerØd（B/A）向新仙女木时期的（YD）过渡期间，东亚冬季风（EAWM）的加强促进了北部冷空气团向南侵入印度支那半岛，冷却了安达曼海。同时，$\delta^{18}O_{sw}$ 的富集是由于印度夏季风（ISM）减弱导致当地降雨量和伊洛瓦底江流入量减少的结果。借助同位素支持的气候模型，我们的结果进一步证明，在 B/A-YD 转换期间，EAWM 和 ISM 的变化与大西洋经向翻转环流（AMOC）的变化密切相关，证实了其在最后一次冰消期间热带印度洋水气候千年尺度变化中的关键作用。

ABSTRACT: In the Indian monsoon realm, spatial homogeneity of hydroclimate response to glacial abrupt climate events in the North Atlantic Ocean and its underlying mechanism are contentious. Here we reconstruct sea surface temperature (SST) and seawater oxygen isotope ($\delta^{18}O_{sw}$) in the central Andaman Sea, which span over the past 26,000 years, to investigate the potential driving mechanism of millennial-scale climate changes in tropical Indian Ocean. Our results demonstrate that millennial-scale SST and $\delta^{18}O_{sw}$ changes during the last deglaciation are associated with changes in Asian monsoon system which follows North Atlantic climate changes. In particular, during the transition from BØlling/AllerØd (B/A) to Younger Dryas (YD), the strengthening of East Asian winter monsoon (EAWM) promotes southward invasion of northern

cold air masses to Indo-China Peninsula, cooling the Andaman Sea. Meanwhile, the enriching $\delta^{18}O_{sw}$ is a consequence of reducing local rainfall amount and Irrawaddy River inflow due to a weakening Indian summer monsoon (ISM). With aid of an isotope-enabled climate model, our results further demonstrate that the changes in EAWM and ISM during B/A-YD transition are closely coupled with variations of Atlantic meridional overturning circulation (AMOC), corroborating its pivotal role in millennial-scale changes in tropical Indian Ocean hydroclimate during the last deglaciation.

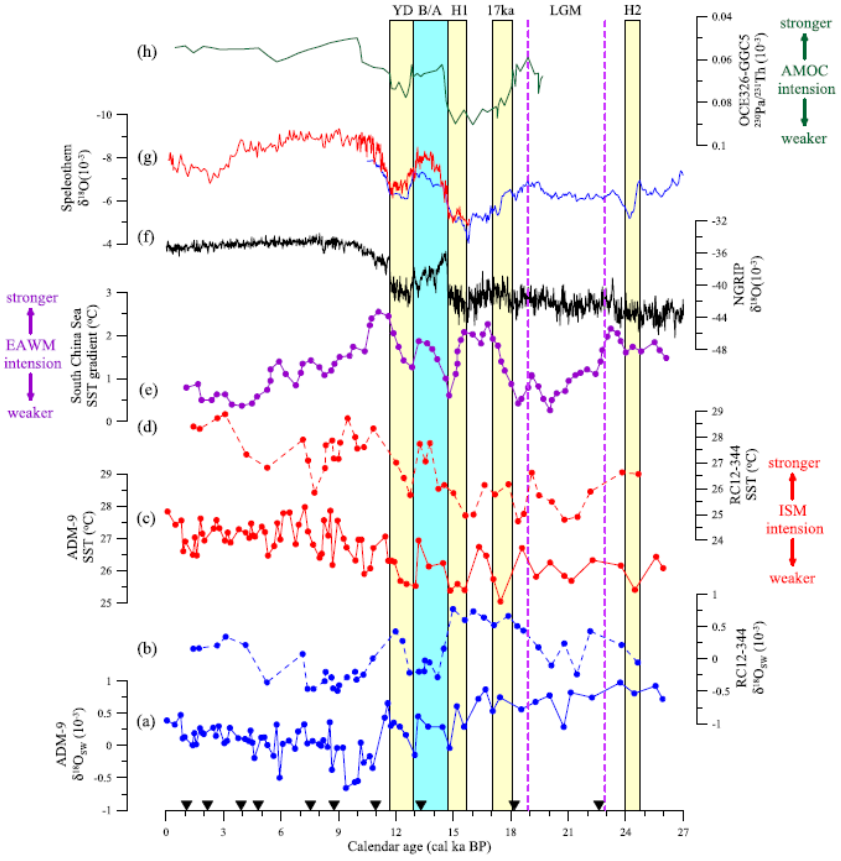

Figure 1. Calendar age (cal ka BP)-dependent plots of paleoclimatic proxies and references: (a) Reconstructed $\delta^{18}O_{sw}$ from our studied core ADM-9; (b) Reconstructed $\delta^{18}O_{sw}$ from core RC12-344; (c) Reconstructed SST (_C) from our studied core ADM-9; (d) Reconstructed SST (_C) from core RC12-344; (e) SST gradient index for EAWM in the South China Sea; (f) $\delta^{18}O$ archives from Greenland NGRIP ice core; (g) Speleothem $\delta^{18}O$ archives from South China's Dongge Cave and from East China's Hulu Cave; (h) AMOC intensity reconstruction using $_{231}Pa/_{230}Th$ proxy from the western subtropical Atlantic.

7. 加拿大 Baffin 岛古新世溢流玄武岩喷发速率、节奏及地层学研究

翻译人：张伟杰 12031188@mail.sustech.edu.cn

Biasi, J., Asimow, P., Horton, F., Boyes, X., et al. ***Eruption rates, tempo, and stratigraphy of Paleocene flood basalts on Baffin Island, Canada****[J].* *Geochemistry, Geophysics, Geosystems, 2022:23, e2021GC010172.*

https://doi.org/10.1029/2021GC010172

摘要：地幔柱高温熔融产生大量的喷发物质在时间上往往与大规模灭绝相一致。古新世 Baffin 岛熔岩是冰岛地幔柱早期活动的产物，其地球化学特征得到了很好的约束，但其地层学、地质年代学和喷发节奏的约束很差。为了提供更好的地质背景，我们测量了七个火山沉积物的地层剖面，并对 38 个熔岩和下覆白垩纪沉积物采点开展了古地磁学研究。本研究的平均古磁极数据足够分散，可以平均掉地磁场长期变化，但其与 60 Ma 时稳定的北美地区的磁极并不重合。在排除了其他可能性之后，我们发现苦橄岩可能是在小于 5 kyr 的极性转换期间喷发的。如果这样的话，对于暴露的最厚的熔岩序列来说，每个熔岩流的平均喷发间隔是~67 年。我们还计算出，溢流玄武岩的最小总体积为 176 km^3（不包括 Baffin 湾水下的熔岩）。这意味着其最小的喷发率为 0.035 km^3/年，这与西格陵兰熔岩流喷发速率相似，但低于较大的溢流玄武岩的喷发速率。尽管如此，Baffin 岛和西格陵兰岛的熔岩在时间上与“C27n 末事件”（全球变暖 2℃）相关，可能是其本质原因。

ABSTRACT: High-temperature melting in mantle plumes produces voluminous eruptions that are often temporally coincident with mass extinctions. Paleocene Baffin Island lavas—products of early Iceland mantle plume activity—are exceptionally well characterized geochemically but have poorly constrained stratigraphy, geochronology, and eruptive tempos. To provide better geologic context, we measured seven stratigraphic sections of the volcanic deposits and collected paleomagnetic data from 38 sites in the lavas and underlying Cretaceous sediments (Quqaluit Fm.). The average paleomagnetic pole from this study does not overlap with the expected pole for a stable North American locality at 60 Ma, yet the data have sufficient dispersion to average out secular variation.

After ruling out other possibilities, we find that the picrites were probably erupted during a polarity transition, over less than 5 kyr. If so, the average eruption interval was ~67 years per flow for the thickest sequence of exposed lavas. We also calculate that the flood basalts had a minimum total volume of ~176 km^3 (excluding submerged lavas in Baffin Bay). This implies a minimum eruption rate of ~0.035 km^3yr^{-1}, which is similar to rates found in West Greenland lavas but less than rates found in larger flood basalts. Despite this, the Baffin and West Greenland lavas temporally correlate with the 'End C27n event' (a period of ~2 ºC global warming) and may be its underlying cause.

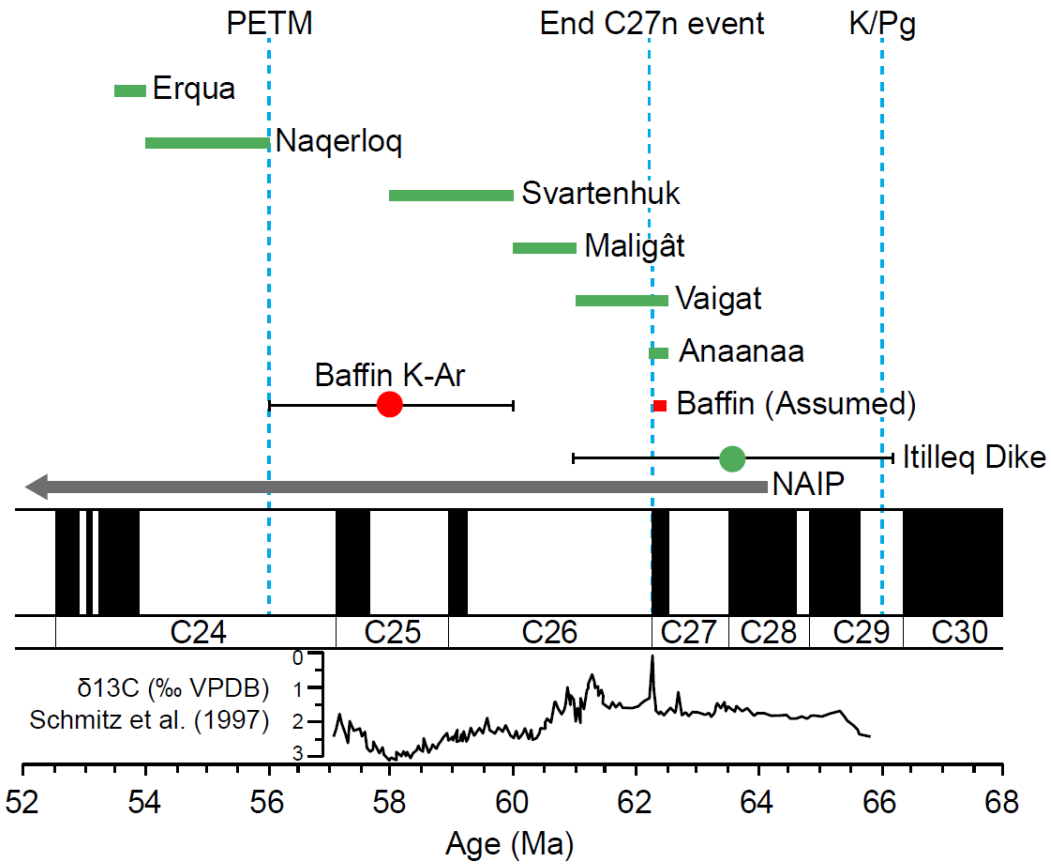

Figure 1. Compilation of geochronological data from the Paleocene Baffin lavas (PBL, red), West Greenland lavas (WGL, green), and the North Atlantic Igneous Province (NAIP). Magnetic polarity timescale from Ogg (2020), Baffin K-Ar age from Clarke and Upton (1971), WGL data from Larsen et al. (2016) and references therein, Paleocene-Eocene Thermal Maximum (PETM) age from Ogg (2020), End C27n event age from Dinarès-Turell et al. (2012), $\delta^{13}C$ values from Schmitz et al. (1997), Cretaceous-Paleogene boundary age from Ogg (2020).

8. 北半球冰川作用加剧促进帕米尔西缘晚上新世黄土的持续堆积

翻译人：李海 12031330@mail.sustech.edu.cn

Zan J, Ning W, Heller F, et al. ***Intensified Northern Hemisphere glaciation facilitates continuous accumulation of late Pliocene loess on the western margin of the Pamir*** *[J]. Geophysical Research Letters, e2022GL099629.*

https://doi.org/10.1029/2022GL099629

摘要：中亚（CA）干旱区的风成黄土序列包含了丰富的中纬度西风带强度变化和区域沙漠干旱化历史的信息。在本研究中，详细的岩性和磁地层研究表明，帕米尔高原西缘的黄土沉积在 2.7 Ma 左右开始积累，代表了 CA 西部最完整和最古老的黄土-古土壤序列。该地区广泛分布的连续黄土沉积表明，CA 在晚上新世快速干旱。欧亚大陆晚新生代风成沉积的初始时间和空间分布进一步表明全球冰量的急剧增加是欧亚大陆、中国和欧洲风成沉积扩张的主要原因，而中更新世扩张是建立欧亚黄土带现代分布格局的重要前提。

ABSTRACT: Thick eolian loess sequences in arid Central Asia (CA) contain a wealth of information on the intensity variations of midlatitude westerlies and the aridification history of the nearby deserts. In this study, detailed lithologic and magnetostratigraphic investigations suggest that loess deposits on the western margin of the Pamir Plateau began to accumulate at around 2.7 Ma, representing the most complete and oldest loess-paleosol sequence in western CA. The widely distributed continuous loess deposition in the region suggests a rapid desiccation of CA during the late Pliocene. A synthesis of the initial timing and spatial distribution of late Cenozoic eolian deposits on the Eurasian continent further demonstrates that the dramatic increase in global ice volume exerted a dominant role in the expansion of eolian loess deposits in CA, China, and Europe, and middle Pleistocene expansion is a crucial precondition for the establishment of modern distribution patterns of the Eurasian loess belt.

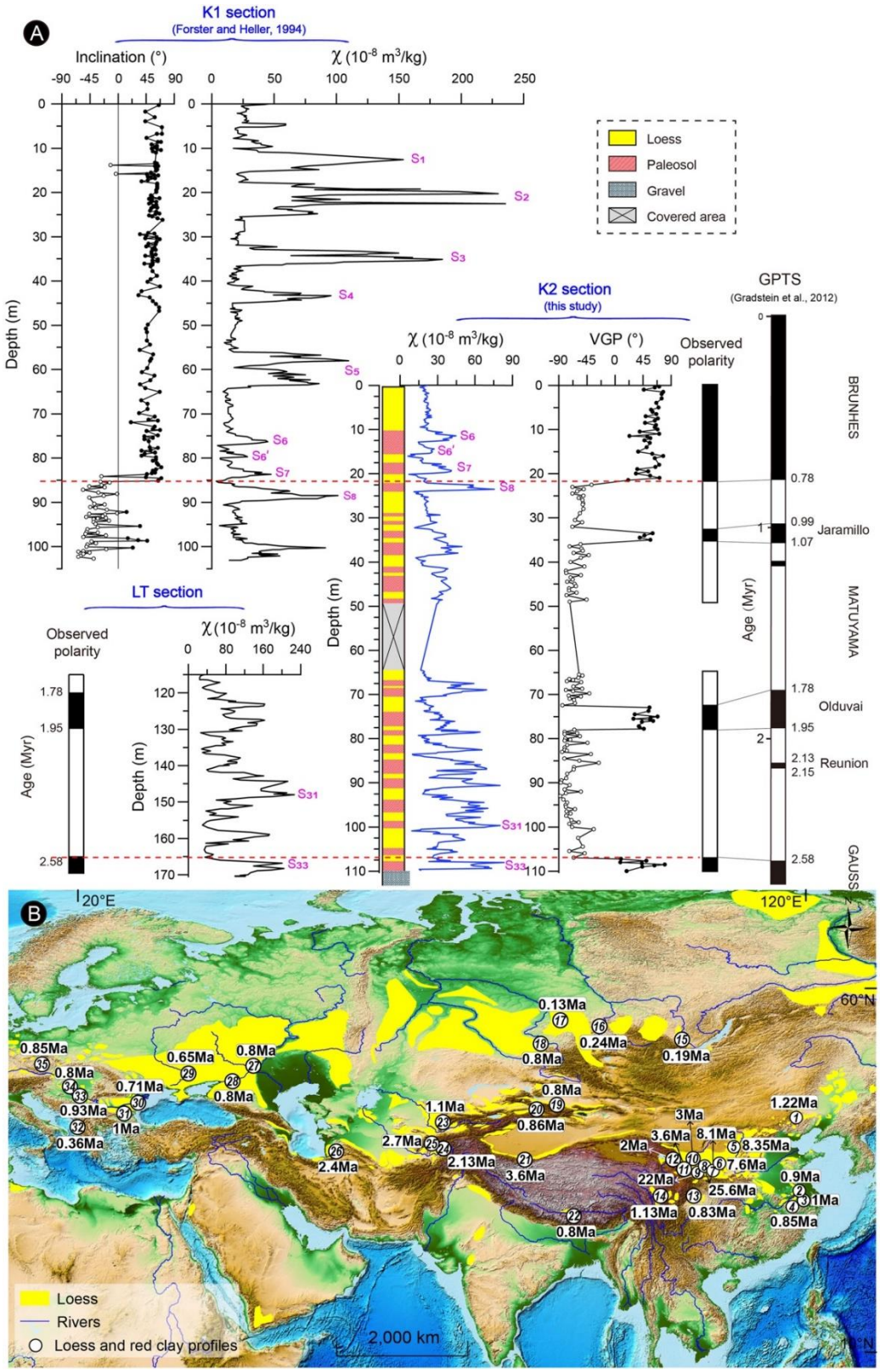

Figure 1. (a) Magnetostratigraphic and magnetic susceptibility records of the K2 loess profile and their correlation with those of the K1 section in southern Tajikistan (Forster & Heller, 1994) and the Lingtai (LT) section on the CLP (Yang & Ding, 2010). The geomagnetic polarity timescale (GPTS)

used for correlation is from Gradstein et al. (2012). Note that the magnetostratigraphic and magnetic susceptibility records of the upper and lower parts of the K2 section are well correlated with those of the K1 section and the Lingtai section, respectively. (b) Synthesis of onset and spatial distribution of late Cenozoic eolian deposits in China, CA, and Europe. The loess distribution in Eurasia follows references of Dodonov (2007), Muhs (2007), and Y. Li et al. (2020). Loess-paleosol and red clay profiles: 1-Sanbahuo and Toudaojingzi (Zeng et al., 2016); 2-Qingshan and Dagang (X. Li et al., 2018); 3-Qiliting (Liu et al., 2008); 4-Xuancheng (Qiao et al., 2003); 5-Jiaxian (Qiang et al., 2001); 6-Xifeng (D. Sun et al., 1998); 7-Chaona (Song et al., 2005); 8-Zhuanglang (Qiang et al., 2011); 9-Qin'an (Z. Guo et al., 2002); 10-Gaolanshan (B. Guo et al., 2020); 11-Guonigou and Nalesi (Zan et al., 2018); 12-Panzishan and Dadunling (Lu et al., 2012); 13-Huagai (Yang et al., 2010); 14-Ganzi (Yan et al., 2001); 15-Igetei and Mal'ta (Chlachula, 2003); 16-Kurtak (Chlachula, 2003); 17-Berezov (Chlachula, 2003); 18-Belovo (Virina et al., 2000); 19-Dongwan (Fang et al., 2002); 20-Talede (Song et al., 2021); 21-Pulu (Fang et al., 2020); 22-Xietongmen (Jin et al., 2000); 23-Khumsan (Lazarenko et al., 1981); 24-Chashmanigar (Nazarov et al., 2020); 25-Karamaidan (this study); 26-Sections east of the Caspian Sea (Wang et al., 2016); 27-Sebryakovo-Mikhailovka (Velichko et al., 2006); 28-Strelitsa (Velichko et al., 2006); 29-Stary Kaydaky (Buggle et al., 2009); 30-Mircea Vodan (Buggle et al., 2009); 31-Viatovo (Jordanova et al., 2008); 32-Ruma (Marković et al., 2006); 33-Titel-Stari Slankamen (Song et al., 2017); 34-Paks (Sartori et al., 1999); 35-Cerveny Kopec (Forster et al., 1996).

9. 西南太平洋过去 14 万年的海冰变化

翻译人：张亚南 zhangyn3@mail.sustech.edu.cn

Jones J, Kohfeld K E, Bostock H, et al. ***Sea ice changes in the southwest Pacific sector of the Southern Ocean during the last 140 000 years*** *[J]. Climate of the Past, 2022, 18, 465-483.*

https://doi.org/10.5194/cp-18-465-2022

摘要：南大洋海冰扩张通过抑制海-气交换和影响海洋经向翻转环流，来调控冰期-间冰期大气 CO_2 变化。然而，由于过去 140 ka 海冰覆盖范围数据的限制，阻碍了我们对认识海冰扩张与影响大气 CO_2 浓度的海洋过程之间联系的能力。根据硅藻组合对过去海冰变化的评估主要集中在末次盛冰期至全新世，很少扩展到冰川终止期II（135 ka）。文中，作者通过现代模拟技术（modern analog technique, MAT）对 TAN1302-96 孔的硅藻化石组合进行了分析，从而展示出西南太平洋整个冰期-间冰期旋回中冬季海冰范围和夏季海洋表面温度（SSST）。作者研究了海冰变化与海洋环流变化在时间上的联系，以及前人提出的冰期早期 CO_2 下降的机制。而后，对比模拟 SSST 与区域 SSST 的变化，从而更好理解表面温度变化对海洋吸收 CO_2 的影响。研究表明，在冰期早期到 MIS 4 期间，研究站位冬季海冰均不存在，意味着海冰可能不是影响冰期早期 CO_2 变化的主要原因。但冰期-间冰期旋回中海冰的扩张与南极中层水（AAIW）的形成和下沉减少相吻合，表明海冰可能影响到中层海洋环流的变化。作者观察到冰期早期（MIS 5d）42-59° S 间的温度梯度减弱，并可能通过影响海-气交换而促进大气 CO_2 的降低

ABSTRACT: Sea ice expansion in the Southern Ocean is believed to have contributed to glacial–interglacial atmospheric CO_2 variability by inhibiting air–sea gas exchange and influencing the ocean's meridional overturning circulation. However, limited data on past sea ice coverage over the last 140 ka (a complete glacial cycle) have hindered our ability to link sea ice expansion to oceanic processes that affect atmospheric CO_2 concentration. Assessments of past sea ice coverage using diatom assemblages have primarily focused on the Last Glacial Maximum (~21 ka) to Holocene, with few quantitative reconstructions extending to the onset of glacial Termination II (~135 ka).

Here we provide new estimates of winter sea ice concentrations (WSIC) and summer sea surface temperatures (SSST) for a full glacial–interglacial cycle from the southwestern Pacific sector of the Southern Ocean using the modern analog technique (MAT) on fossil diatom assemblages from deep-sea core TAN1302-96. We examine how the timing of changes in sea ice coverage relates to ocean circulation changes and previously proposed mechanisms of early glacial CO_2 drawdown. We then place SSST estimates within the context of regional SSST records to better understand how these surface temperature changes may be influencing oceanic CO_2 uptake. We find that winter sea ice was absent over the core site during the early glacial period until MIS 4 (~65 ka), suggesting that sea ice may not have been a major contributor to early glacial CO_2 drawdown. Sea ice expansion throughout the glacial–interglacial cycle, however, appears to coincide with observed regional reductions in Antarctic Intermediate Water production and subduction, suggesting that sea ice may have influenced intermediate ocean circulation changes. We observe an early glacial (MIS 5d) weakening of meridional SST gradients between 42 and 59° S throughout the region, which may have contributed to early reductions in atmospheric CO_2 concentrations through its impact on air–sea gas exchange.

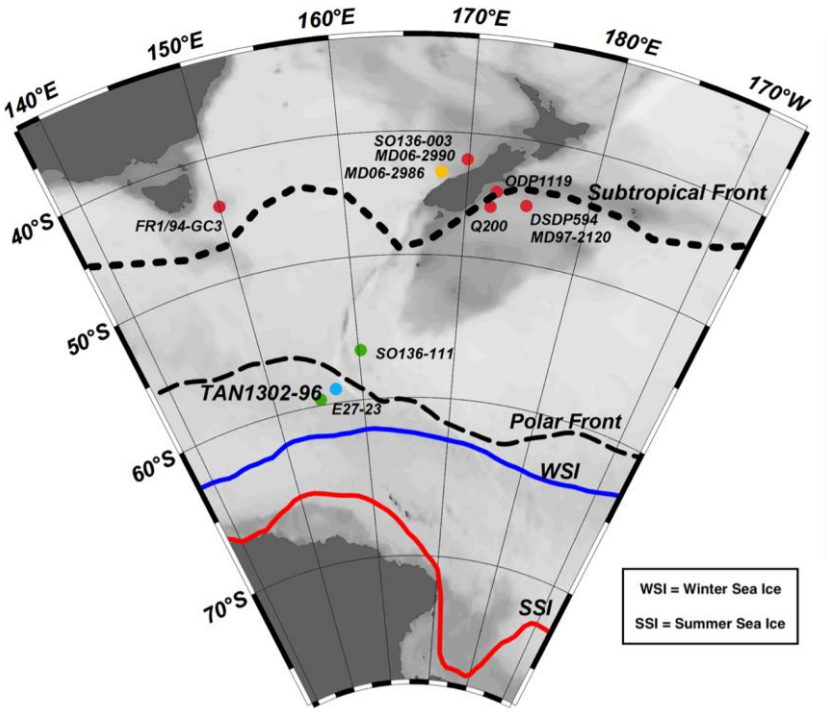

Figure 1. Map of the southwestern Pacific sector of the Southern Ocean including the study site, TAN1302-96 (blue circle), and additional published cores providing sea ice extent data, SO136-111

and E27-23 (green circles); SST reconstructions (red circles); and $\delta^{13}C$ of benthic foraminifera (yellow circles). Note that some cores may not appear present in the figure because of their proximity to other cores. Data for all cores are provided in Table 2. Dashed lines show the average location of the subtropical and polar fronts (Smith et al., 2013; Bostock et al., 2015), and red and blue lines show mean positions of modern summer sea ice (SSI) and winter sea ice (WSI) extents, respectively (Reynolds et al., 2002, 2007).

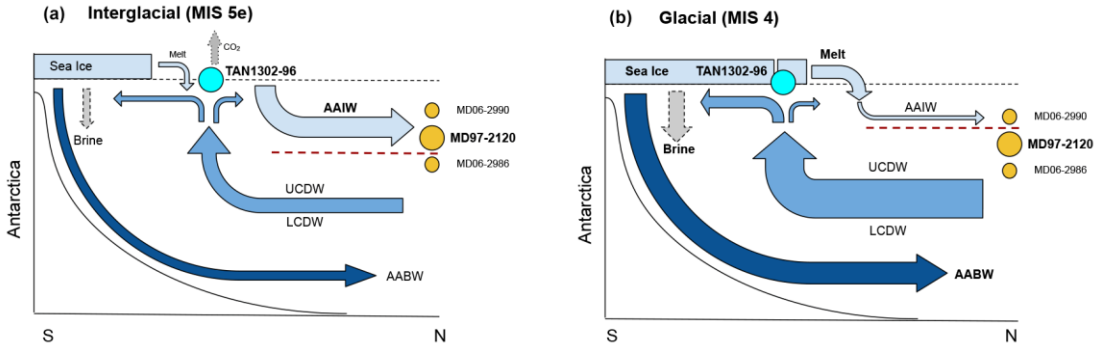

Figure 2. Schematic of changes in southwestern Pacific sector sea ice coverage and water mass geometry between interglacial and glacial stages. Panel (a) depicts interglacial conditions where sea ice coverage is minimal and freshwater input from summer sea ice melt is low. This lack of freshwater input allows AAIW to subduct to deeper depths and bath core MD97-2120, capturing the higher δ13C signature of the overlying AAIW waters. The AAIW-UCDW interface (red dashed line) is located beneath MD97-2120. CO_2 outgassing is occurring as a carbon-rich Circumpolar Deep Water upwell near Antarctica. Panel (b) depicts glacial conditions where sea ice expansion has occurred beyond TAN1302-96, increasing brine rejection, and stabilizing the water column. As a result of the increased sea ice growth, subsequent summer melt increases the freshwater flux into the AAIW source region and increases AAIW buoyancy. This buoyancy gain shoals the AAIW-UCDW interface above core MD97-2120, causing the core site to be bathed in low $\delta^{13}C$ UCDW. The shoaling of AAIW causes an indirect expansion of CDW, increasing the glacial carbon stocks of the deep ocean, while sea ice reduces CO_2 outgassing via the capping mechanism.

10. 在大西洋发现独特的岩石圈-软流圈边界和古登堡不连续面

翻译人：刘宇星 11811211@mail.sustech.edu.cn

Pranav Audhkhasi, Satish C. Singh. ***Discovery of distinct lithosphere-asthenosphere boundary and the Gutenberg discontinuity in the Atlantic Ocean****[J]. Science Advances, 2022, 8(24): abn5404.*
https://doi.org/10.1126/sciadv.abn5404

摘要：板块构造理论要求刚性岩石圈漂浮在弱软流圈之上，由岩石圈-软流圈边界隔开，该边界有时被称为古腾堡不连续面。利用深地震反射技术，我们发现了大西洋中 27 Ma 至 58 Ma 海洋岩石圈中两个连续反射层的存在。我们发现上部反射层随着年龄的增加而变深并遵循~1250˚C 等温线，而更深的反射位于~75 km 的恒定深度。我们认为上反射代表热控岩石圈-软流圈边界，而下反射是古腾堡不连续面，这是一个类似冻干的脱水边界，将上方的干地幔熔融区与下方在脊轴处形成的水合地幔分开。我们还发现地幔热异常会使岩石圈恢复活力，抬升岩石圈-软流圈边界，并破坏古腾堡不连续面。

ABSTRACT: The plate tectonic theory requires a rigid lithosphere floating over a weak asthenosphere, separated by the lithosphere-asthenosphere boundary, which has been sometimes interpreted as the Gutenberg discontinuity. Using a deep seismic reflection technique, we report the presence of two continuous reflections covering 27 Ma to 58 Ma oceanic lithosphere in the Atlantic Ocean. We find that the upper reflection deepens with age and follows the ~1250°C isotherm, whereas the deeper reflection lies at a constant depth of ~75 km. We suggest that the upper reflection represents the thermally controlled lithosphere-asthenosphere boundary, whereas the lower reflection is the Gutenberg discontinuity, a frozen-in dehydration boundary separating the dry mantle melting region above from the hydrated mantle below formed at the ridge axis. We also find that thermal mantle anomalies rejuvenate the lithosphere, uplift the lithosphere-asthenosphere boundary, and destroy the Gutenberg discontinuity.

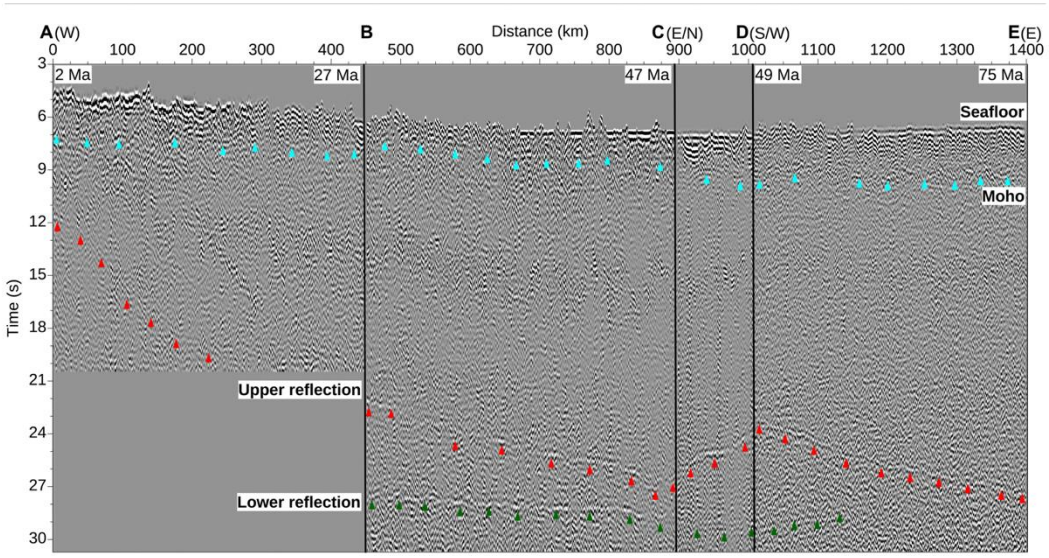

Figure 1. Seismic reflection image in the time domain. Final seismic image in TWTT along the profile after extensive processing (see Materials and Methods). The segment boundaries along the profile are demarcated by solid black vertical lines at points B (27 Ma), C (47 Ma), and D (49 Ma). The seafloor, Moho (cyan arrows), and upper (red) and lower (green) mantle reflections have been marked. The blow-ups of the individual segments A-B, B-C, and C-E are shown in figs. S17, S18, and S19, respectively.

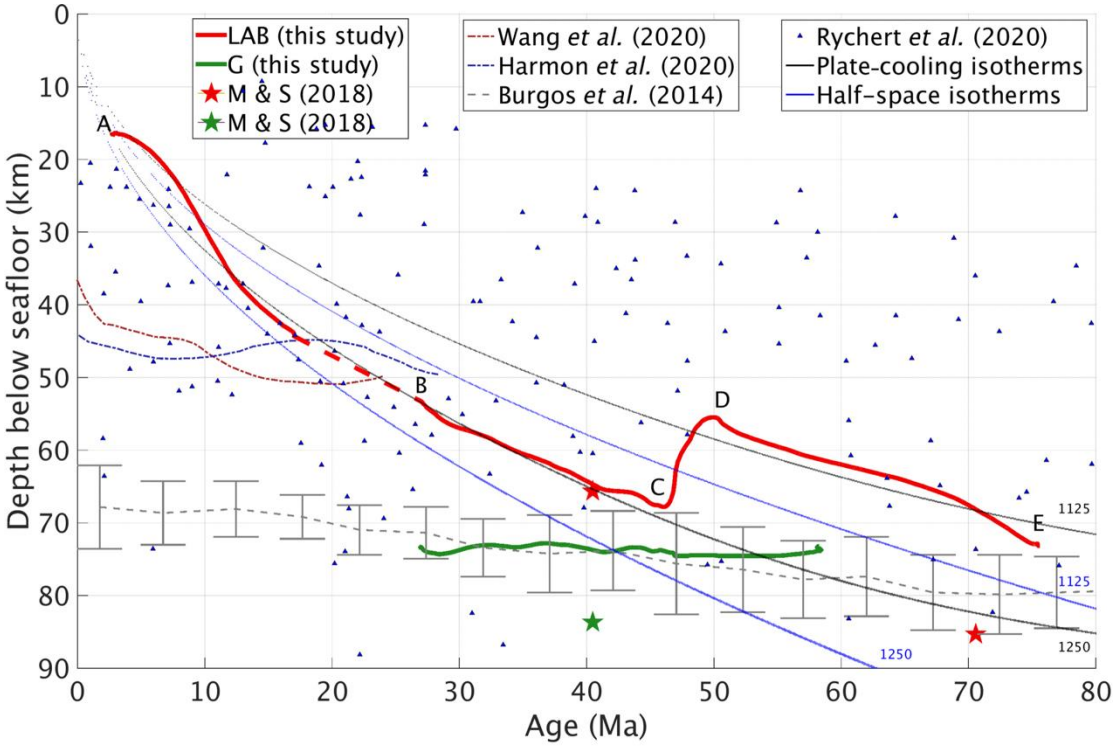

Figure 2. Depth-converted image. Depth-converted mantle reflections, interpreted as the LAB (red) and G-reflection (green). Red dashed line indicates the interpolated depth from 16 Ma to 27 Ma.

Best-fitting half-space (solid blue) and plate-cooling (solid black) isotherms are also plotted (1, 53) and have an uncertainty of ±20°C. Results from seismic reflection study across the St. Paul fracture zone are shown by red (top) and green (bottom) stars at 40 Ma and 70 Ma, respectively (13). Dashed gray line with error bars indicates the results from radial anisotropy in the Atlantic Ocean (3). The blue triangles indicate the ensemble of LAB depths observed from previous studies (10) showing widespread LAB depths. Recent results from surface wave tomography (solid dotted blue line) (4) and colocated magnetotelluric experiment (solid dotted brown line) (29) just south of Chain fracture zone have also been plotted. The surface wave tomography and magnetotelluric results have a depth uncertainty of ≥10 to 15 km (4, 29).